molecules

MDPI

Article

Synthesis and Characterization of an α-Fe_2O_3-Decorated g-C_3N_4 Heterostructure for the Photocatalytic Removal of MO

Rooha Khurram [1], Zaib Un Nisa [2], Aroosa Javed [3], Zhan Wang [1,*] and Mostafa A. Hussien [4,5,*]

[1] Beijing Key Laboratory for Green Catalysis and Separation, Department of Chemistry and Chemical Engineering, Beijing University of Technology, Beijing 100124, China; khurramrooha@emails.bjut.edu.cn
[2] Department of Chemistry, School of Natural Sciences (SNS), National University of Sciences and Technology (NUST), H-12, Islamabad 44000, Pakistan; zaibunisadab@gmail.com
[3] Department of Chemistry, University of Calgary, Calgary, AB T2N 1N4, Canada; aroosa.899@gmail.com
[4] Department of Chemistry, Faculty of Science, King Abdulaziz University, Jeddah P.O. Box 80203, Saudi Arabia
[5] Department of Chemistry, Faculty of Science, Port Said University, Port Said 42521, Eygpt
* Correspondence: wangzh@bjut.edu.cn (Z.W.); maabdulaal@kau.edu.sa (M.A.H.)

Abstract: This study describes the preparation of graphitic carbon nitride (g-C_3N_4), hematite (α-Fe_2O_3), and their g-C_3N_4/α-Fe_2O_3 heterostructure for the photocatalytic removal of methyl orange (MO) under visible light illumination. The facile hydrothermal approach was utilized for the preparation of the nanomaterials. Powder X-ray diffraction (XRD), Scanning electron microscopy (SEM), Energy dispersive X-ray (EDX), and Brunauer–Emmett–Teller (BET) were carried out to study the physiochemical and optoelectronic properties of all the synthesized photocatalysts. Based on the X-ray photoelectron spectroscopy (XPS) and UV-visible diffuse reflectance (DRS) results, an energy level diagram vs. SHE was established. The acquired results indicated that the nanocomposite exhibited a type-II heterojunction and degraded the MO dye by 97%. The degradation ability of the nanocomposite was higher than that of pristine g-C_3N_4 (41%) and α-Fe_2O_3 (30%) photocatalysts under 300 min of light irradiation. The formation of a type-II heterostructure with desirable band alignment and band edge positions for efficient interfacial charge carrier separation along with a larger specific surface area was collectively responsible for the higher photocatalytic efficiency of the g-C_3N_4/α-Fe_2O_3 nanocomposite. The mechanism of the nanocomposite was also studied through results obtained from UV-vis and XPS analyses. A reactive species trapping experiment confirmed the involvement of the superoxide radical anion ($O_2^{\bullet-}$) as the key reactive oxygen species for MO removal. The degradation kinetics were also monitored, and the reaction was observed to be pseudo-first order. Moreover, the sustainability of the photocatalyst was also investigated.

Keywords: g-C_3N_4; g-C_3N_4/α-Fe_2O_3 nanocomposite; MO photodegradation; heterostructure (type-II); alignment of energy levels

check for updates

Citation: Khurram, R.; Nisa, Z.U.; Javed, A.; Wang, Z.; Hussien, M.A. Synthesis and Characterization of an α-Fe_2O_3-Decorated g-C_3N_4 Heterostructure for the Photocatalytic Removal of MO. *Molecules* **2022**, *27*, 1442. https://doi.org/10.3390/molecules27041442

Academic Editor: Andrea Bencini

Received: 15 January 2022
Accepted: 16 February 2022
Published: 21 February 2022

1. Introduction

Although synthetic dyes provide vibrant colors, they also cause serious water pollution problems. Dye wastewater produced by textile, paper, leather, and other industries has become one of the main sources of water pollution [1]. Among the synthetic dyes, anionic azo dyes account for half of dye synthesis and industrial application [2]. Due to their low coloring rate on natural fibers, anionic dyes account for a large proportion of the dye wastewater discharged by printing and dyeing factories. Methyl orange (MO) is a common and typical azo anionic dye. This water-soluble organic synthetic dye has very high colorability and presents a bright orange color when dissolved in water. Azo dyes, such as methyl orange, contain aromatic and –N = N– groups in their molecules, which are highly toxic, carcinogenic, and teratogenic [3,4], and are harmful to the environment and organisms [5]; thus, wastewater must be treated innocuously before it can be discharged. MO was selected as a model pollutant in this study.

In recent years, various semiconductor-based photocatalysts have been designed to perform photocatalytic tasks, including H_2 production, CO_2 reduction, dye degradation, etc. [6]. Despite several attempts at improvement, their performances are not satisfactory owing to the weak separation of the light-generated charge carriers with limited light-harvesting efficiency. In 2009, one of the most well-known metal-free polymeric photocatalysts, called g-C_3N_4, was employed in H_2 production via water splitting by Wang et al. [7]. Afterward, this photocatalyst earned enormous attention in CO_2 reduction and pollutant degradation, owing to suitable bandgap (2.6–2.7 eV) and band edge positions, chemical stability, and cost-effectivity [8–13]. However, the efficiency of pristine g-C_3N_4 is unacceptable due to its poor visible light absorption and high charge carrier recombination [14]. Various strategies, including composite formation, doping, and utilizing any photosensitizer, have been employed to address these issues [15,16]. Hematite (α-Fe_2O_3) is considered a promising n-type semiconductor, exhibiting a suitable band potential for efficient light absorption at a wide range of wavelengths [17]. Moreover, α-Fe_2O_3 possesses special characteristics, including tremendous stability, non-toxicity, photocurrent and corrosion resistance, etc. [18]. Therefore, two-component g-C_3N_4 based systems are synthesized to form heterojunction structures with a higher photocatalytic efficiency utilizing a wide wavelength range [19]. Thus far, various reports have published the Z-scheme action and heterojunction mechanism of the g-C_3N_4/α-Fe_2O_3 composite in pollutant degradation [20], CO_2 reduction [21–23], photoelectrochemical [24,25], Hg (II) reduction [26], etc. However, there are few reports comprising the ternary and quaternary systems of g-C_3N_4/α-Fe_2O_3 for the degradation of wastewater dyes following the heterojunction mechanism [20]. The charge transfer between the interfacial phase in potential photocatalytic mechanisms may follow the typical heterojunction mechanism or Z-scheme mechanism. In the typical heterojunction mechanism, the sample absorbs visible light, which stimulates the migration of electrons from the VB to the CB, leaving h^+ in the VB. Subsequently, h^+ from constituent-1 migrates to the E_{VB} of constituent-2, and e^- from constituent-2 transfers to the E_{CB} of constituent-1. Different from the typical heterojunction photogenerated electrons and photogenerated holes, the e^- generated in the CB of constituent-1 moves directly to combine with the h^+ in the VB of constituent-2. The photogenerated e^- in the CB of constituent-2 participates in the reduction reaction, while the h^+ generated in the VB of constituent-1 participates in the oxidation of water. Thus, the electron transfer pathway presents a Z-shaped path. As a result of both potential photocatalytic mechanisms, the efficiency of electron-hole transfer and separation are promoted and the recombination rates of photoexcited electron-hole pairs in both constituents themselves are inhibited. However, the redox potential values with respect to the conduction and valence band position of photocatalysts play a critical role in determining the type of potential photocatalytic mechanisms. For instance, in their first report, Xu. Q. et al. investigated the superior photocatalytic performance of 2D/2D α-Fe_2O_3/g-C_3N_4 for H_2 generation through the Z-scheme mechanism [27]. In another report, Jiang, Z. et al. developed a hierarchical Z-scheme over an α-Fe_2O_3/g-C_3N_4 hybrid for enhanced CO_2 reduction [28]. In both these studies, the authors investigated the Z-scheme for efficient photocatalytic performance. However, the authors did not investigate the involvement of reactive oxygen species that are involved in photocatalytic activity. Recently, Mohsen Padervand et al. [29] studied the formation of ROS where ·OH radicals were fundamentally involved in RhB degradation under light, suggesting a Z-scheme mechanism.

Owing to insufficient literature on the mechanistic investigation of type-II heterostructures to better understand ROS involvement, this novel work chose to investigate their formation by conducting an active species trapping experiment. The synthesis of an efficient g-C_3N_4/α-Fe_2O_3 heterostructure was conducted via a facile hydrothermal approach utilizing cost-effective precursors. The photocatalytic efficiency was estimated by the photodegradation of methyl orange (MO) dye under visible light illumination. The reactive species trapping experiment revealed the formation of superoxide radical anions $O_2^{\bullet -}$ as primary species for MO removal. Moreover, kinetic studies were conducted to determine

the order of the reaction. The results of XPS and UV-vis spectroscopy were utilized for drawing the band alignment vs. SHE. The band diagram illustrating the band edge position was developed and elaborated.

2. Results and Discussion

2.1. Physiochemical and Optoelectronic Properties of All the Synthesized Photocatalysts

Typical XRD patterns of g-C_3N_4, α-Fe_2O_3, and g-C_3N_4/α-Fe_2O_3 are displayed in Figure 1. The XRD pattern of pure g-C_3N_4 exhibits an intense, broad, asymmetric, and characteristic peak at 27.4° indexed as the (002) diffractions for the graphitic interlayer stacking of the conjugated aromatic ring. A less intense peak at a lower angle of 13.1° was indexed as the (100) diffractions for the inter-planar stacking peaks of the tri-s-triazine units. Both the corresponding peaks perfectly matched with the JCPDS no. 87–1526. g-C_3N_4 was found to have a hexagonal crystal structure [30,31]. Pure α-Fe_2O_3 exhibited diffraction peaks at Bragg's angle 24.2°, 33.2°, 35.6°, 40.9°, 49.5°, 54.1°, 58°, 62°, 63° indexed as (012), (104), (110), (113), (024), (116), (018), (214), and (300) diffractions, respectively, which were perfectly in accordance with the JCPDS card # 01-089-0598 for its rhombohedral crystal system [32]. In addition, the peaks of both the individual constituents, i.e., g-C_3N_4 and α-Fe_2O_3, could be seen in the XRD pattern of the g-C_3N_4/α-Fe_2O_3 composite, indicating the successful in-situ synthesis of the nanocomposite and thereby endorsing the phase purity. Moreover, in the g-C_3N_4/α-Fe_2O_3 XRD pattern, no obvious peak shifting occurred, indicating that the crystal structure was maintained during the synthesis process.

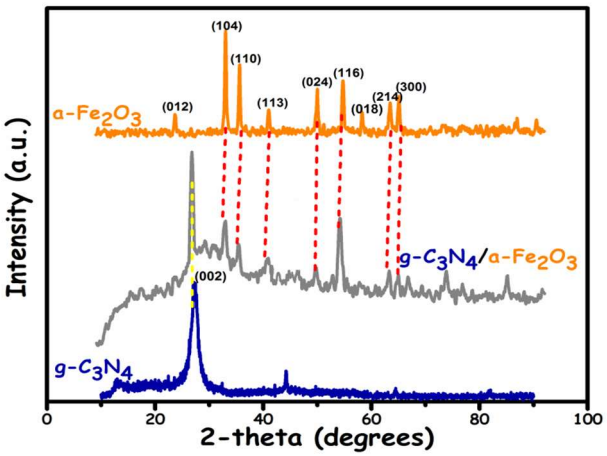

Figure 1. The XRD patterns.

The crystallite size was also calculated from the XRD results. The estimated average crystallite sizes of g-C_3N_4/α-Fe_2O_3, g-C_3N_4, and α-Fe_2O_3 were 60.5 nm, 29.4 nm, and 32.5 nm, respectively, calculated using Equation (1). Crystallite size has been recognized as an important parameter that influences the photocatalytic performance of the material [33]. The recombination of the photogenerated charge carriers by the photocatalyst sample critically depends on its crystallite size [34]. The charge carrier recombination process may be carried out in two ways: volume recombination or surface recombination [35]. Surface recombination is the dominant process in smaller crystallites. For pure/bare samples (e.g., g-C_3N_4 and α-Fe_2O_3), the charge carrier's mobility becomes extremely low and undergoes recombination before it can reach the surface. Both g-C_3N_4 and α-Fe_2O_3 exhibit a small crystallite size, i.e., 29.4 nm and 32.5 nm, respectively; therefore, most of the charge carriers are generated sufficiently close to the surface. As a result, the photogenerated charge carriers that reach the surface result in faster recombination. This is also owing to the lack of driving force to separate the charge carriers. Further interfacial charge transfer processes will be outweighed by the surface recombination rate for smaller crystallites [35]. However, the g-C_3N_4/α-Fe_2O_3 nanocomposite exhibits a larger crystallite size, i.e., 60.5 nm. In this case, a driving force to separate the charge carriers exists. Thereby, a reduction in

this surface recombination results in a reduced recombination rate of the photogenerated charge carriers and hence results in greater efficiency. Thus, a higher photocatalytic activity is observed for the nanocomposite.

The morphological analysis was carried out by scanning electron microscopy, and the results are displayed in Figure 2. The SEM micrograph displays the laminar nanosheet-like structure of pure g-C_3N_4 and the agglomerated nanoparticle-like structure of α-Fe_2O_3. A laminar-nanosheet like morphology provides abundant active sites and space for the attachment of α-Fe_2O_3. Figure 2c shows the morphology of the nanocomposite. The g-C_3N_4 nanosheet was fully and randomly decorated with α-Fe_2O_3 nanoparticles. This close and strong interaction may have been established between g-C_3N_4 and α-Fe_2O_3, which facilitate the charge carriers' separation and transfer for an improved photocatalytic response. However, in the future, this should be further confirmed through HR-TEM analysis.

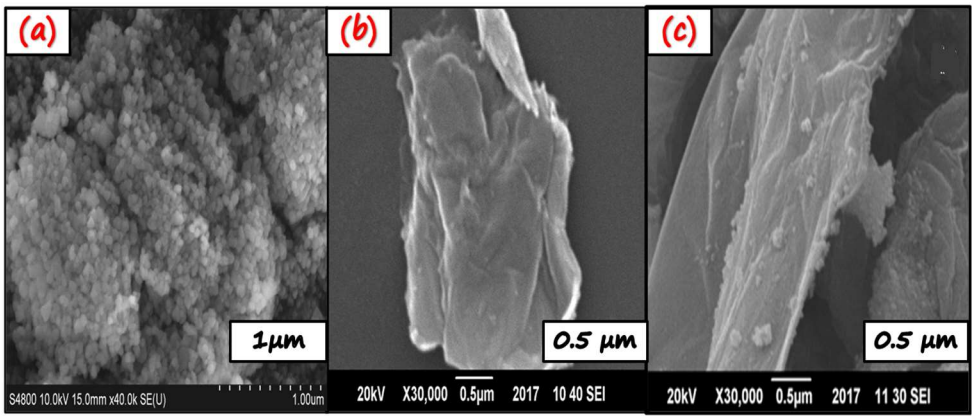

Figure 2. SEM micrographs of (**a**) α-Fe_2O_3 agglomerated nanoparticles, (**b**) g-C_3N_4 crumpled nanosheet, and (**c**) g-C_3N_4/α-Fe_2O_3 nanosheet well decorated with nanoparticles.

The composition and elemental distribution of the synthesized photocatalysts were investigated by EDS, and the results are presented in Figure 3. The EDS analysis also confirmed the purity of all the synthesized samples. The EDS spectra of g-C_3N_4 indicated carbon and nitrogen as primary elements, as shown in Figure 3a. Figure 3c shows the distinct peaks of Fe and O for the α-Fe_2O_3 sample. The EDS spectrum (Figure 3b) demonstrated the distribution of C, N, Fe, and O elements without any impurity, confirming the phase purity of the synthesized α-Fe_2O_3/g-C_3N_4 nanocomposite, as supported by the XRD patterns. The weight percentage and atomic percentage of all the samples are also depicted in Figure 3.

XPS analysis was performed to examine the surface chemistry, elemental composition, and electronic states of all the elements, and the outcomes are depicted in Figure 4. Figure 4a depicts the C 1s spectrum comprising two peaks. The peak located at 284.8 eV was attributed to sp^2 hybridized C-C, while the second peak at 288.3 eV was attributed to sp^2 hybridized C atoms in the aromatic ring (N=C-N) [36,37]. On the contrary, the deconvoluted N 1s spectrum (Figure 4b) depicted four distinct peaks at 398.6, 399.9, 400.4, and 404.4 eV, which were ascribed to sp^2 hybridized N in the triazine ring (C=N-C groups), tertiary N-atoms bonded to carbon (N-$(C)_3$ groups), the amino group of N-H, and the charging effect in the heterocycles, respectively [38,39]. The typical α-Fe_2O_3 spectra (Figure 4c) showed two distinct peaks at 710.7 and 724 eV corresponding to Fe $2p_{3/2}$ and Fe $2p_{1/2}$, respectively. Two shake-up satellite peaks characteristic of the 3^+ oxidation state of Fe in α-Fe_2O_3 following each distinct peak at 718.9 and 732.9 eV were also seen. The O 1s spectra (Figure 4d) showed a distinct peak at 529.5 eV and a shake-up satellite peak at 531.9 eV, corresponding to the crystal lattice 2^- oxygen and a surface hydroxyl group, respectively [40].

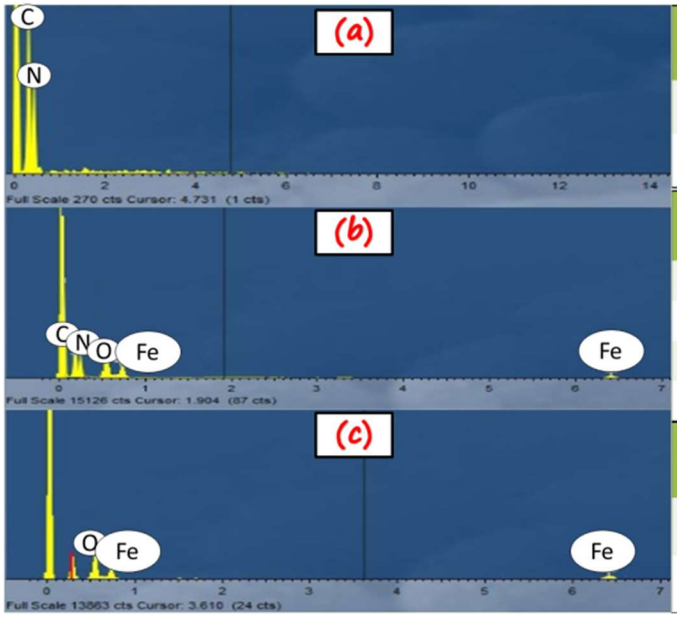

Element	Weight %	Atomic %
N	66.64	63.14
C	33.36	36.86

Element	Weight %	Atomic %
N	7.81	17.05
C	5.18	9.81
Fe	45.23	49.94
O	41.61	23.20

Element	Weight %	Atomic %
Fe	69.63	39.64
O	30.37	60.36

Figure 3. EDS spectra of: (**a**) g-C_3N_4, (**b**) α-Fe_2O_3, and (**c**) g-C_3N_4/α-Fe_2O_3 with quantification of atomic percentages.

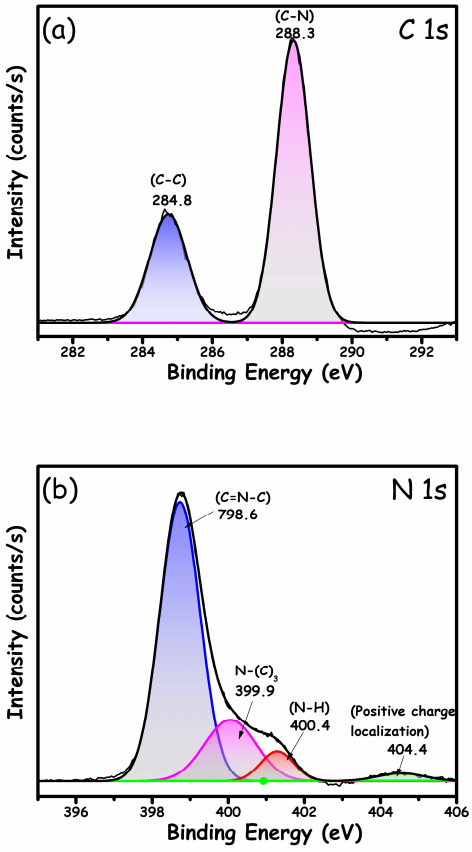

Figure 4. *Cont.*

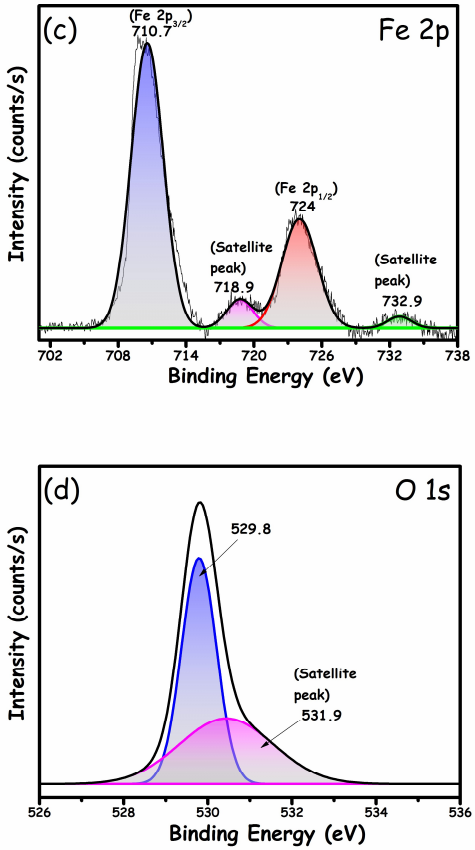

Figure 4. XPS spectra of g-C_3N_4/α-Fe_2O_3 nanocomposite: (**a**) C (1s), (**b**) N (1s), (**c**) Fe (2p), and (**d**) O (1s).

Surface area critically affects photocatalytic performance. Therefore, specific surface area measurements and pore size were investigated through N_2 adsorption–desorption isotherms (Figure 5). All sample exhibited type IV isotherms. The results demonstrated that the surface area of the g-C_3N_4/α-Fe_2O_3 nanocomposite was significantly larger than its individual constituents, i.e., α-Fe_2O_3 and g-C_3N_4. However, the surface area of the g-C_3N_4 nanosheets was higher than that of α-Fe_2O_3. This might be attributed to the laminar sheet-like morphology of g-C_3N_4 or the aggregation of α-Fe_2O_3 nanoparticles, which lowers its surface area. From greatest to smallest, the surface areas of the prepared photocatalysts were as follows: α-Fe_2O_3/g-C_3N_4 > g-C_3N_4 > α-Fe_2O_3 (Figure 5a). However, the literature reveals conflicting results regarding the surface area analysis of the combination of α-Fe_2O_3 and g-C_3N_4. For example, Li et al. [41] synthesized an α-Fe_2O_3/g-C_3N_4 nanocomposite by the pyrolysis of melamine, and ferric nitrate showed an increment in surface area compared to pure g-C_3N_4. However, Sun et al. [42] prepared an α-Fe_2O_3/g-C_3N_4 nanocomposite by using precursors, including ferric chloride and dicyandiamide. Their results were antagonistic to the traditional trend: the surface area of pure g-C_3N_4 was reduced. Zhang et al. [43] reported no noticeable change in the surface area of g-C_3N_4 when the α-Fe_2O_3/g-C_3N_4 nanocomposite was synthesized by the direct mixing of α-Fe_2O_3 and g-C_3N_4. This indicates that the nanocomposite synthesis procedure plays a dominating role in determining its textural properties that influence its surface area. In this study, the surface area of the nanocomposite increased to 80.38 m^2/g, almost one-fold greater than pristine g-C_3N_4. On the other hand, the surface area measurements for the g-C_3N_4 and α-Fe_2O_3 were 39.89 m^2/g and 34.25 m^2/g, respectively. Our findings are in good agreement with the reported studies of Li et al. [41]. A larger surface area increases the available active sites and effectively promotes adsorption and desorption, thereby enhancing the photocatalytic response. The relevant pore diameter distribution the of samples exhibited a broad distribution between 10 and 50 nm, which is characteristic of mesopores (Figure 5b). The broad distribution of pores included small and large mesopores. The smaller pores indicate the nanoporous

structure on the surface of g-C_3N_4 nanosheets and other nanoparticles, and the larger pores are related to those formed from randomly stacked layers of graphitic carbon nitride. The porous structure should facilitate the fast transmission of reactants and products during the photocatalytic reaction process.

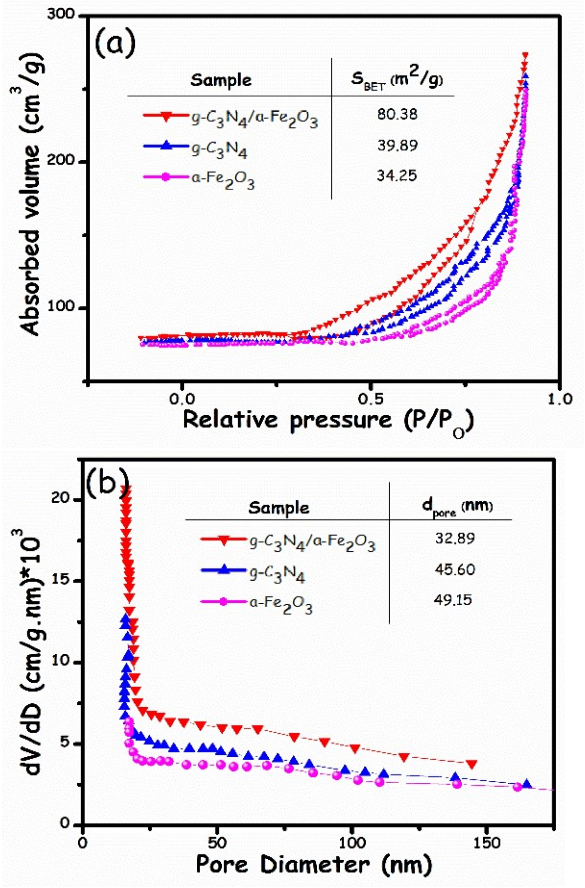

Figure 5. (**a**) N_2 adsorption–desorption isotherms and (**b**) pore size distributions of α-Fe_2O_3, g-C_3N_4, and α-Fe_2O_3/g-C_3N_4 samples.

2.2. Photocatalytic Performance for MO Degradation

The activity of the g-C_3N_4/α-Fe_2O_3 nanocomposite was evaluated by the photodegradation of MO under light. Figure 6 demonstrates the comparative analysis of spectral changes over pristine g-C_3N_4 and the g-C_3N_4/α-Fe_2O_3 nanocomposite. For pure g-C_3N_4 (Figure 6a), the intensity of the maximum absorption peak (λ_{max}) of MO at 464 nm decreased slowly, indicating that the degradation rate of MO was relatively slow, which signified the presence of non-degraded MO molecules even after 300 min of reaction time. However, the g-C_3N_4/α-Fe_2O_3 nanocomposite (Figure 6b) peak at λ_{max} decreased gradually within 300 min, indicating its superior photocatalytic performance. The spectral change over the time for pure g-C_3N_4 and the g-C_3N_4/α-Fe_2O_3 nanocomposite was correlated with its photocatalytic performance. The photocatalytic degradation ability of g-C_3N_4/α-Fe_2O_3 was two-fold higher than that of pure g-C_3N_4. This improvement in photocatalytic degradation could be attributed to the decreasing electron-hole recombination rate and expanded surface area.

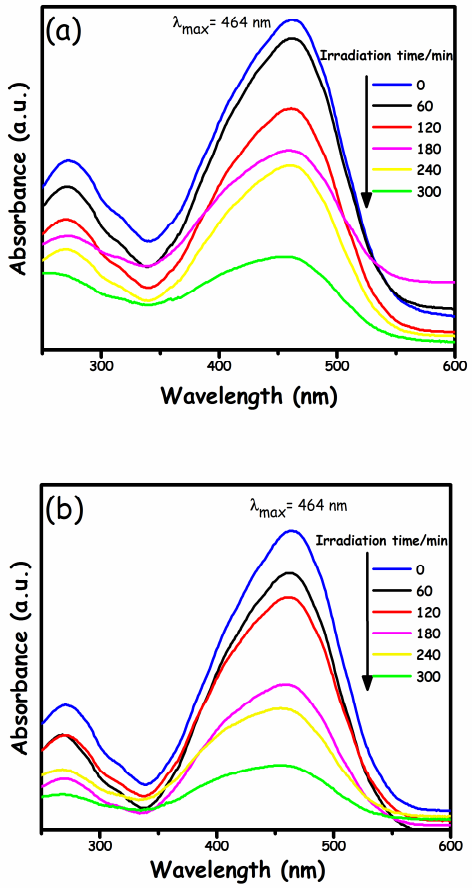

Figure 6. UV-vis absorption spectral changes of MO with time in (**a**) pure g-C_3N_4 and (**b**) g-C_3N_4/α Fe_2O_3 nanocomposite under light illumination.

The detailed photocatalytic degradation performance for all the prepared pure and composite photocatalysts was further investigated and is illustrated in Figure 7. A control experiment was also carried out in the absence of a photocatalyst, depicting an almost negligible degradation. Figure 7a represents the change of MO concentration vs. irradiation time under visible light for 5 h. The results revealed that the percentage of MO removal by the g-C_3N_4/α-Fe_2O_3 nanocomposite was superior, followed by pristine g-C_3N_4 and α-Fe_2O_3, degrading 97, 41, and 30% of the MO, respectively, as shown in the degradation plot in Figure 7b. The enhanced degradation efficiency of the g-C_3N_4/α-Fe_2O_3 nanocomposite might be credited to the type-II heterostructure and enhanced surface area. This heterostructure results in enhanced charge carrier separation at the heterojunction interface.

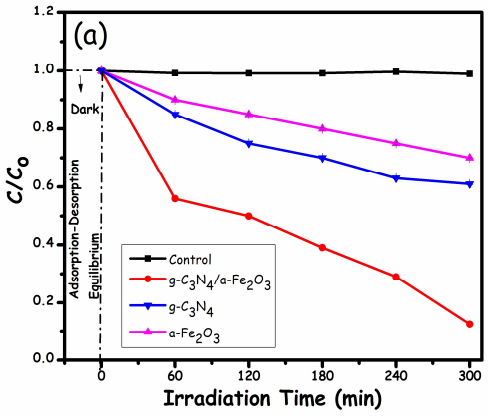

Figure 7. *Cont.*

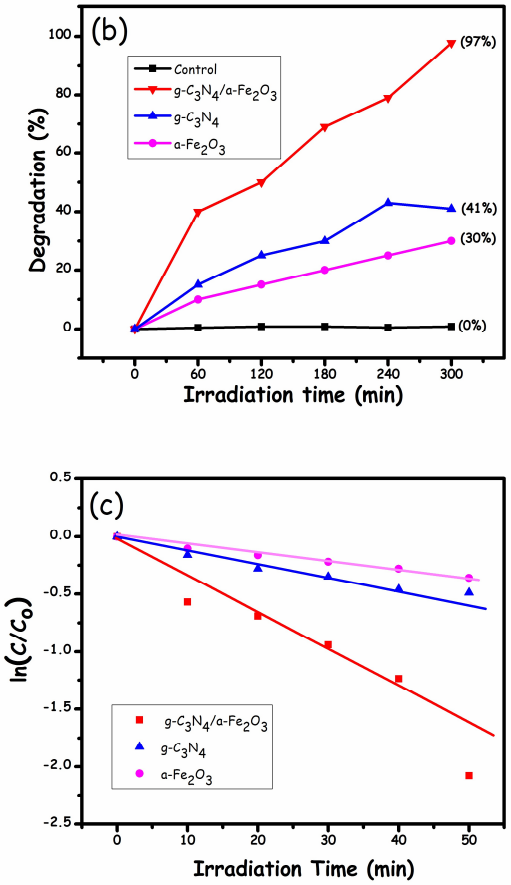

Figure 7. (**a**) Plot of C/C_o vs. time. (**b**) The corresponding degradation efficiency of MO removal. (**c**) Plot of ln (C/C_o) vs. time.

Furthermore, a higher surface area increases the number of available active sites for the absorption and degradation of MO. Moreover, the kinetics of the degradation reaction were also determined, as shown in Figure 7c. The kinetic spectra depict the occurrence of pseudo-first order reactions with all the photocatalysts.

Table 1 summarizes all the prepared photocatalysts' precise results, including the percentage composition found via EDX, the crystallite size calculated using the XRD values, the bandgap (eV) value ascertained from DRS data, the surface area estimated through BET analysis, and the photocatalytic efficiency.

Table 1. Summary of all characterization techniques.

S#	Sample Code	EDX—Percentage Composition				XRD—Avg. Crystallite Size (nm)	DRS—Band Gap (eV)	BET—Surface Area (m^2/g)	Photocatalytic Efficiency (%)
		Atomic % of C	Atomic % of N	Atomic % of O	Atomic % of Fe				
1	$g\text{-}C_3N_4$	36.86	63.14	—	—	29.4	2.62	39.89	41
2	$\alpha\text{-}Fe_2O_3$	—	—	60.36	39.64	32.5	2.1	34.25	30
3	$g\text{-}C_3N_4/\alpha\text{-}Fe_2O_3$	9.81	17.05	23.20	49.94	60.5	—	80.38	97

2.3. Photocatalytic MO Degradation Mechanism

The band edge position plays a critical role in determining the reaction mechanism. In this study, XPS was used to calculate the valence band (VB) positions along with UV-visible-DR spectroscopy to ascertain the band gap energies of $\alpha\text{-}Fe_2O_3$ and $g\text{-}C_3N_4$, and the results are shown in Figure 8. Based on the acquired results, the valence band maximum (VBM) was found to be 1.48 eV and 1.60 eV for $g\text{-}C_3N_4$ and $\alpha\text{-}Fe_2O_3$, respectively. As the XPS instrument has a work function of 4.62 eV, the final VBM values were estimated to be

1.6 and 1.72 eV against SHE (as 0 V against SHE is equivalent to 4.5 eV against a vacuum) for g-C_3N_4 and α-Fe_2O_3, respectively. Furthermore, the conduction band minimum (CBM) of the component photocatalysts was calculated using the following equation:

$$E_{CB} = E_{VB} - E_g \quad (1)$$

Band gaps (*E*g) were estimated utilizing Tauc plots (Figure 8c,d). Figure 8c displays the DRS spectra of g-C_3N_4, showing an optical absorption threshold at 473.2 nm, whereas Figure 8d illustrates the DRS spectra of α-Fe_2O_3, showing an absorption edge at 597.4 nm. The band gaps were calculated to be 2.62 eV and 2.1 eV for g-C_3N_4 and α-Fe_2O_3, respectively, which coincide well with the reported values [40]. Based on these valence band and band gap values, the conduction band values were found to be −1.02 eV vs. SHE for g-C_3N_4 and −0.38 eV vs. SHE for α-Fe_2O_3. Finally, the energy level diagram was drawn (as presented in Figure 9) utilizing the results from Figure 8.

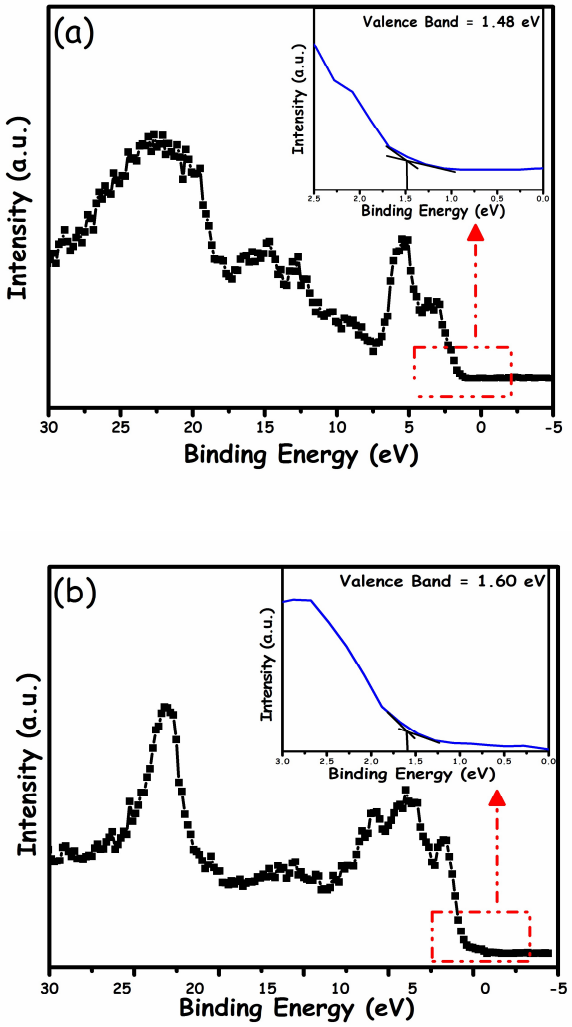

Figure 8. *Cont.*

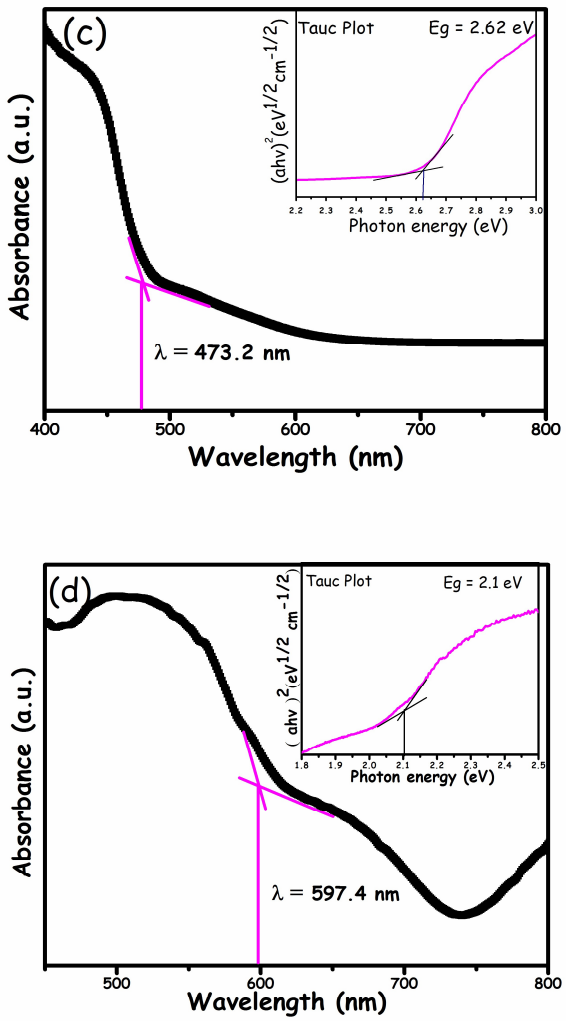

Figure 8. XPS valence band spectra with insets representing magnified spectra of (**a**) g-C_3N_4 and (**b**) α-Fe_2O_3, and absorbance spectra with insets representing the Tauc plots for (**c**) g-C_3N_4 and (**d**) α-Fe_2O_3.

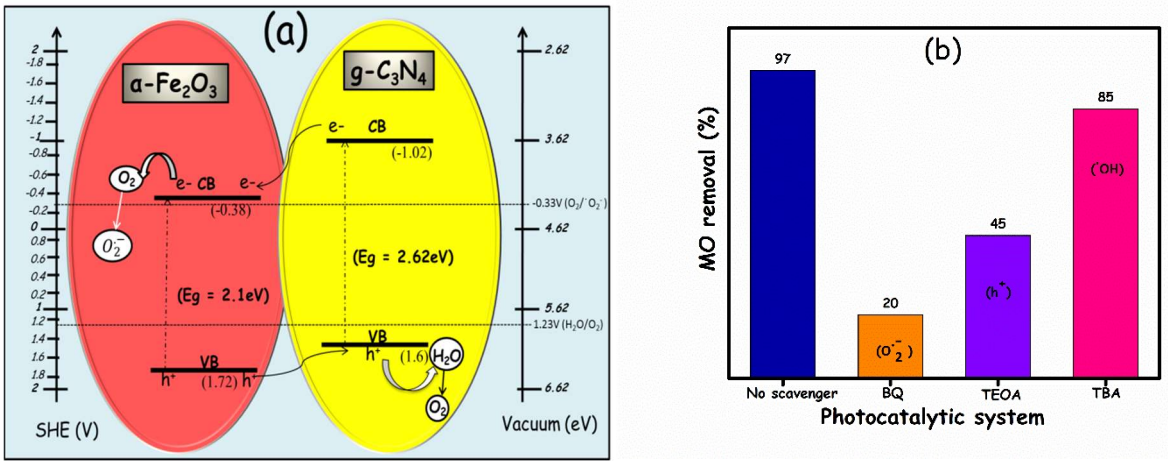

Figure 9. (**a**) Alignment of energy levels in the g-C_3N_4/α-Fe_2O_3 nanocomposite. (**b**) Role of radical scavengers on MO photodegradation over g-C_3N_4/α-Fe_2O_3 nanocomposite.

The alignment of energy levels crucially determines the overall photocatalytic mechanism. When light is turned on, the electrons (e^-) from the valence band of the components

move to their respective conduction bands, leaving behind holes (h^+), as illustrated in Figure 9. The band edge positions are evidence of the formation of the type-II heterostructure, facilitating the e^- and h^+ transfer from one component to other. In this study, the e^- from the conduction band of the g-C_3N_4 jumped to the CB of α-Fe_2O_3, where the reduction of O_2 to the superoxide radical anion ($O_2^{\bullet-}$) takes place. This occurred due to the suitability of the CBM value of α-Fe_2O_3 (−0.38 V vs. SHE) with respect to the value of −0.33 V vs. SHE, which is the reduction potential of $O_2/O_2^{\bullet-}$. This O_2 may have been the dissolved O_2 in the surrounding environment that the experiment was conducted in or the aerobic environment produced as a consequence of H_2O oxidation. On the other hand, the h^+ was transferred from α-Fe_2O_3 to g-C_3N_4. Owing to the more positive band position of g-C_3N_4 compared to the H_2O oxidation potential (1.23 V vs. SHE), the oxidation of water (H_2O) into oxygen (O_2) could be taken into account. This antagonistic movement of e^- and h^+ is also responsible for the remarkable enhancement in photocatalytic activity, as it minimizes the chances of their recombination. In previous studies, the photocatalytic mechanism was reported to be driven by different species. For instance, Sangbin lee et al. observed the photodegradation of methylene blue (MB) via $O_2^{\bullet-}$ over hematite/graphitic carbon nitride composites [44]. Jirong Bai et al. also identified $O_2^{\bullet-}$ as an active species that further degrades rhodamine B (RhB) over α-Fe_2O_3/porous g-C_3N_4 [45]. Konstantinos C. Christoforidis et al. illustrated h^+ as an active species for the degradation of MO over β-Fe_2O_3/g-C_3N_4 hybrid catalysts, while ·OH negligibly takes part in the photocatalytic mechanism [46]. Moreover, Xin Liu et al. [47] proposed a similar mechanism, where $O_2^{\bullet-}$ functions as primary and h+ participates as secondary active species for the degradation of RhB over Fe_2O_3/g-C_3N_4 photocatalysts. Thus, these reported results are consistent with our study, where we believe $O_2^{\bullet-}$ plays a primary role in degradation. The primary role of the superoxide radical anion was further attested by the active species trapping experiment results. The trapping experiments were conducted utilizing scavengers for holes (h^+) and free radicals; the results are presented in Figure 9b. Benzoquinone (BQ), triethanolamine (TEOA), and tert-butyl alcohol (TBA) were utilized as $O_2^{\bullet-}$, h^+, and ·OH scavengers, respectively. A control experiment was conducted where no scavenger is utilized, and 97% of MO removal was observed after 5 h of light illumination. The scavenger concentration employed was 0.1 mM. With the addition of BQ, TEOA, and TBA into the solution, the MO removal efficiency was decreased to 20%, 45%, and 85%, respectively. MO degradation was significantly suppressed when BQ was utilized as a scavenger. Thus, the results of the trapping experiments clearly demonstrate that the hydroxyl radical (·OH) and hole (h^+) play a minor role in the photocatalytic removal of MO, whereas, $O_2^{\bullet-}$ is the primary ROS that further degrades the MO over the g-C_3N_4/α-Fe_2O_3 nanocomposite, which is in good agreement with recent studies [44–47].

Table 2 demonstrates a comparative study of this work with already reported literature.

2.4. Photocatalyst Sustainability

An essential factor towards the practicability of any photocatalyst is its stability. This work determined the stability of the photocatalyst by recycling the catalyst for three cycles followed by centrifugation and washing with DI-water after each cycle, as illustrated in Figure 10. As shown in the graph, the results revealed a decrement in the degradation efficiency by approximately 1.6% after the first cycle and approximately 2% in the third cycle. This decrease in activity might be ascribed to the loss of photocatalyst during washing and the blocking of active sites for the next run. This is justified by the chemical structure of MO dye (Figure 11), as MO dye adsorbs on the catalyst surface through hydrophilic or electrostatic interactions. When washing the photocatalyst after each photodegradation cycle, there is a chance of the incomplete desorption of the sample from the catalyst's surface, which leads to the blockage of active sites for the next cycle, thereby decreasing the photocatalytic activity. In addition, the loss of activity might be related to a progressive inactivation of the catalyst (the loss of active phase or catalyst surface modification) [48].

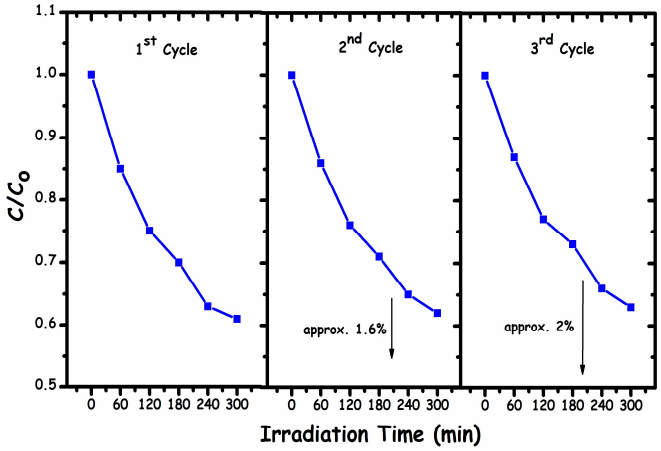

Figure 10. g-C_3N_4/α-Fe_2O_3 nanocomposite stability.

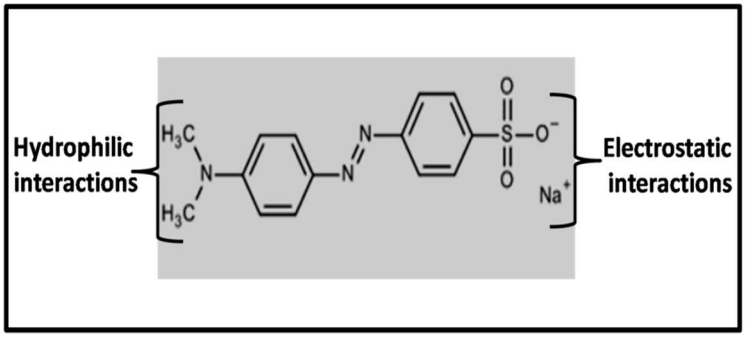

Figure 11. Chemical structure of MO dye.

Table 2. Comparison with literature.

S. No.	Photocatalysts	Irradiation Source	Time	Conc. of Pollutant and Amount of Catalyst	Pollutant Degraded	Degradation Rate/Efficiency (%)	Ref.
1	Fe_2O_3/C_3N_4/Au nanocomposite	-	-	MO solution (25 mL, 3×10^{-3} M) and 10.0 mg of catalyst	MO	-	Nasri, A. et al. [20]
2	α-Fe_2O_3/g-C_3N_4 nanocomposite	30 W LED lamp	3 h	MB aqueous solution (2.12×10^{-5} M) and 5.5 mg L^{-1} of catalyst	MB	66.79%	Navid Ghane et al. [49]
3	α-Fe_2O_3/g-C_3N_4 composite	UV lamps (254 nm, 6 W)	90 min	200 mL of 10 mg/L methylene blue solution	MB	2.6 times higher than bare materials	Sangbin Lee [44]
4	α-Fe_2O_3/porous g-C_3N_4 heterojunction hybrids	500 W Xe arc lamp with 420-nm cut-off filter)	20 min	50 mL of RhB solution and 10 mg/L of catalyst	RhB	91.1%	Jirong Bai et al. [45]
5	ZnO-modified g-C3N4	200 W tungsten lamps	90 min	-	MB	90%	Paul, Devina Rattan et al. [50]
7	Fe_2O_3/g-C_3N_4 hybrid nanocomposite	300 W Xe arc lamp	4 h	160 mL of aqueous solution containing 10 mg L^{-1} of MO	MO	Approx. 80%	Konstantinos C. Christoforidis [46]
8	g-C_3N_4/α-Fe_2O_3 nanocomposite	300 W xenon lamp	5 h	0.01 g of catalyst powder in 50 mL dye solution	MO	97%	This work

3. Materials and Methods

3.1. Chemicals

All the materials and chemicals used for the synthesis were of analytical grade and were used without further purification. Moreover, nanopure water was utilized for the synthesis. Melamine ($C_3H_6N_6$; >99%), ferric nitrate nonahydrate ($Fe(NO_3)_3 \cdot 9H_2O$; >97%), and urea (NH_2CONH_2; 99.5%) were purchased from Sinopharm Chemical Reagent Co., Ltd.

(Huangpu, Shanghai, China). The model pollutant, i.e., methyl orange ($C_{14}H_{14}N_3NaO_3S$), was bought from Beijing Chemical Reagent Limited Corporation in Beijing, China.

3.2. Preparation of α-Fe_2O_3

In a distinctive route, 0.1 M (0.807 g) of ferric nitrate and 0.15 M (0.18 g) of urea were separately dissolved in 20 mL of distilled water and stirred for 15 min. Then, the above two solutions were collectively mixed in a beaker and again stirred for 15 min. The as-prepared mixture was placed in a Teflon-lined sealed autoclave at 100 °C for 8 h. The α-Fe_2O_3 was prepared by utilizing ferric nitrate as a source of iron. Afterwards, the sample was washed several times, centrifuged, and dried in a vacuum oven overnight at 60 °C to obtain deep red-colored α-Fe_2O_3 nanoparticles. We found that the mixture (ferric nitrate and urea) was highly suitable for the preparation of α-Fe_2O_3 nanoparticles. The possible formation mechanism of α-Fe_2O_3 nanoparticles involves a series of chemical reactions (Equations (2)–(4)).

The importance of utilizing urea lies in the fact that for the synthesis of hematite, the basic source and its dosage affect the morphology, e.g., a small amount of urea produces a less hollow and more interconnected morphology while a large amount of urea produces solid hollow microspheres [51]. Upon heating to 70 °C, the dissolved urea decomposes to carbon dioxide and ammonia (Equation (2)). Carbon dioxide (CO_2) bubbles produced during the hydrolyzation play an important role. CO_2 acts as a soft template for the formation of the hollow structure. In our study, since the dosage of urea was only 0.18 g, the amount of CO_2 produced was too minute to form the microbubbles under that situation. Therefore, a more interconnected morphology of the nanoparticles of hematite was obtained. Furthermore, the hydrolysis of ammonia yields the ammonium ion and hydroxyl ion (Equation (3)). The hydroxyl ion reacts with a ferric ion and generates $Fe(OH)_3$, which is the primary growth nucleus with an amorphous structure. The further combination and growth of neighboring primary nuclei leads to the formation of agglomerated hematite NPs [52] (Equation (4)).

$$CH_4N_2O + H_2O \rightarrow CO_2 + 2NH_3 \quad (2)$$

$$NH_3 + H_2O \rightarrow NH_4^+ + OH^- \quad (3)$$

$$Fe^{3+} + OH^- \rightarrow Fe(OH)_3 \rightarrow \alpha - Fe_2O_3 \quad (4)$$

3.3. Preparation of g-C_3N_4

The g-C_3N_4 was synthesized through a simple calcination approach by placing 5 g melamine in a ceramic crucible followed by heating in a muffle furnace at 550 °C at a 3 °C/min ramp rate for 2 h. The resulting yellow-colored g-C_3N_4 precipitates were stored for further experimental use.

3.4. Preparation of g-C_3N_4/α-Fe_2O_3

The synthesis procedure for the fabrication of the g-C_3N_4/α-Fe_2O_3 composite is identical to α-Fe_2O_3 synthesis. Before heating, 0.2 g of as-synthesized g-C_3N_4 was added to the reaction mixture of ferric nitrate and urea followed by ultrasonication for 60 min. Subsequently, the mixture was placed in oven at 100 °C for 8 h. Afterward, the sample was washed with ultrapure water and then with ethanol, followed by centrifugation and drying in a vacuum oven overnight at 60 °C. Finally, the light red colored precipitates were obtained and stored for further characterization.

3.5. Characterization Techniques

The phase purity and structural analysis of as-synthesized photocatalysts were studied by X-ray diffraction spectroscopy (XRD, Cu Kα radiation, Bruker D8) with 2θ range 20°–80°

at a rate of 0.1 °C/min. In addition, the crystallite size of all the catalysts was calculated using Scherrer's formula:

$$D = K\lambda/\beta \cos\theta \quad (5)$$

where K is the shape constant with a value of 0.89, D represents the crystallite size, λ is wavelength (Cu k-alpha generally has a wavelength of 0.15405 nm), β is the full width at half maxima (FWHM) of the observed peak, and θ represents the angle. The morphological analysis was carried out by scanning electron microscopy (SEM; Hitachi S4800), equipped with energy dispersive X-ray spectroscopy analysis, which further justified the samples' composition and purity. The chemical states and valence band positions were determined by X-ray photoelectron spectroscopy (XPS; ESCALAB 250Xi, Al Kα). A UV-vis spectrophotometer (UV-750, Indium as reference) was employed for DRS reflectance spectra. The DRS spectra were transformed to absorption spectra by utilizing the Kubelka–Munk equation:

$$\alpha h\nu^{1/2} = K(h\nu - Eg) \quad (6)$$

where α represents the absorption coefficient, K is the proportional constant, h represents Plank's constant, ν is the vibration frequency, and Eg represents bandgap (eV). Additionally, the BET specific surface area was measured using the nitrogen adsorption–desorption method at 77K (BET, BELSORP-mini II).

3.6. MO Degradation Activity

Methyl orange (MO) was used as a model dye, and its photodegradation response was investigated by utilizing a UV-vis spectrophotometer. The degradation activity was carried out by dispersing 0.01 g of catalyst powder in dye solution with a concentration of 100 ppm. Prior to light exposure, the suspension was placed aside for 20 min in order to develop the adsorption–desorption equilibrium. MOmax was observed at 464 nm. Eventually, the light source was turned on. The light source was a 300 W xenon lamp (number of the lamp was 2) with a cut-off filter (>420 nm) with an output power density of 100 mW/cm^2, which was placed at a distance of 15 cm from the vessel containing the dye solution. Three milliliters of the irradiated suspension were collected at various time intervals, followed by centrifugation to analyze the dye concentration. Moreover, a control experiment was also carried out in light but without any catalyst and is labeled as control in the photocatalytic degradation plots.

4. Conclusions

The domain of developing nanocomposites to stop recombination for a higher photocatalytic response has already been well established. The novelty of this study lies in its investigation of the mechanistic route and type of reactive oxygen species involved in the photodegradation of MO, utilizing a g-C_3N_4/α-Fe_2O_3 nanocomposite. Based on the results of the characterization assays, the energy level diagram and suitable band edge positions vs. SHE justify this study. The g-C_3N_4/α-Fe_2O_3 nanocomposite showed a superior photocatalytic response towards the photodegradation of MO than its individual counterparts. The redox potential values with respect to the valence and conduction band values suggest a potentially heterojunction-based photocatalyst mechanism. Additionally, the kinetics of the degradation reactions were also monitored. Moreover, the photocatalyst sustainability experiment depicted the practical application of this nanocomposite. In the future, the potentially potent g-C_3N_4/α-Fe_2O_3 nanocomposite can be utilized for other photocatalytic applications, including CO_2 reduction or photoelectrochemical studies.

Author Contributions: Conceptualization, R.K.; methodology, R.K.; formal analysis, R.K.; writing—original draft, R.K.; writing—review and editing, Z.U.N., A.J., M.A.H. and Z.W.; resources, Z.U.N. and A.J.; funding acquisition, M.A.H.; supervision, Z.W. All authors have read and agreed to the published version of the manuscript.

Funding: This research received no external funding.

Institutional Review Board Statement: Not applicable.

Informed Consent Statement: Not applicable.

Data Availability Statement: Not applicable.

Acknowledgments: First author would like to acknowledge Saqib Ali for continuous support during this work.

Conflicts of Interest: The authors declare that there is no conflict of interest.

Sample Availability: Not applicable.

References

1. Tkaczyk, A.; Mitrowska, K.; Posyniak, A. Synthetic organic dyes as contaminants of the aquatic environment and their implications for ecosystems: A review. *Sci. Total Environ.* **2020**, *717*, 137222. [CrossRef] [PubMed]
2. Chang, J.-S.; Lin, C.-Y. Decolorization kinetics of a recombinant Escherichia coli strain harboring azo-dye-decolorizing determinants from *Rhodococcus* sp. *Biotechnol. Lett.* **2001**, *23*, 631–636. [CrossRef]
3. Bai, Y.-N.; Wang, X.-N.; Zhang, F.; Wu, J.; Zhang, W.; Lu, Y.-Z.; Fu, L.; Lau, T.-C.; Zeng, R.J. High-rate anaerobic decolorization of methyl orange from synthetic azo dye wastewater in a methane-based hollow fiber membrane bioreactor. *J. Hazard. Mater.* **2020**, *388*, 121753. [CrossRef] [PubMed]
4. Haque, M.M.; Haque, M.A.; Mosharaf, M.K.; Marcus, P.K. Decolorization, degradation and detoxification of carcinogenic sulfonated azo dye methyl orange by newly developed biofilm consortia. *Saudi J. Biol. Sci.* **2021**, *28*, 793–804. [CrossRef]
5. Kant, R. Textile dyeing industry an environmental hazard. *Nat. Sci.* **2011**, *4*, 17027. [CrossRef]
6. Khurram, R.; Javed, A.; Ke, R.; Lena, C.; Wang, Z. Visible Light-Driven GO/TiO_2-CA Nano-Photocatalytic Membranes: Assessment of Photocatalytic Response, Antifouling Character and Self-Cleaning Ability. *Nanomaterials* **2021**, *11*, 2021. [CrossRef]
7. Wang, X.; Maeda, K.; Thomas, A.; Takanabe, K.; Xin, G.; Carlsson, J.M.; Domen, K.; Antonietti, M. A metal-free polymeric photocatalyst for hydrogen production from water under visible light. *Nat. Mater.* **2009**, *8*, 76–80. [CrossRef]
8. Xia, P.; Zhu, B.; Yu, J.; Cao, S.; Jaroniec, M. Ultra-thin nanosheet assemblies of graphitic carbon nitride for enhanced photocatalytic CO_2 reduction. *J. Mater. Chem. A* **2017**, *5*, 3230–3238. [CrossRef]
9. Masih, D.; Ma, Y.; Rohani, S. Graphitic C3N4 based noble-metal-free photocatalyst systems: A review. *Appl. Catal. B Environ.* **2017**, *206*, 556–588. [CrossRef]
10. Fu, J.; Zhu, B.; Jiang, C.; Cheng, B.; You, W.; Yu, J. Hierarchical porous O-doped g-C3N4 with enhanced photocatalytic CO_2 reduction activity. *Small* **2017**, *13*, 1603938. [CrossRef]
11. Lin, L.; Ou, H.; Zhang, Y.; Wang, X. Tri-s-triazine-based crystalline graphitic carbon nitrides for highly efficient hydrogen evolution photocatalysis. *ACS Catal.* **2016**, *6*, 3921–3931. [CrossRef]
12. Cheng, F.; Yin, H.; Xiang, Q. Low-temperature solid-state preparation of ternary CdS/g-C_3N_4/CuS nanocomposites for enhanced visible-light photocatalytic H_2-production activity. *Appl. Surf. Sci.* **2017**, *391*, 432–439. [CrossRef]
13. Li, K.; Su, F.-Y.; Zhang, W.-D. Modification of g-C3N4 nanosheets by carbon quantum dots for highly efficient photocatalytic generation of hydrogen. *Appl. Surf. Sci.* **2016**, *375*, 110–117. [CrossRef]
14. Kang, Y.; Yang, Y.; Yin, L.C.; Kang, X.; Liu, G.; Cheng, H.M. An amorphous carbon nitride photocatalyst with greatly extended visible-light-responsive range for photocatalytic hydrogen generation. *Adv. Mater.* **2015**, *27*, 4572–4577. [CrossRef]
15. Zhong, X.; Jin, M.; Dong, H.; Liu, L.; Wang, L.; Yu, H.; Leng, S.; Zhuang, G.; Li, X.; Wang, J.-G. TiO_2 nanobelts with a uniform coating of g-C_3N_4 as a highly effective heterostructure for enhanced photocatalytic activities. *J. Solid State Chem.* **2014**, *220*, 54–59. [CrossRef]
16. Nguyen, C.-C.; Do, T.-O. Engineering the high concentration of N_3C nitrogen vacancies toward strong solar light-driven photocatalyst-based g-C_3N_4. *ACS Appl. Energy Mater.* **2018**, *1*, 4716–4723. [CrossRef]
17. Sivula, K.; Le Formal, F.; Grätzel, M. Solar water splitting: Progress using hematite (α-Fe_2O_3) photoelectrodes. *ChemSusChem* **2011**, *4*, 432–449. [CrossRef]
18. Spray, R.L.; McDonald, K.J.; Choi, K.-S. Enhancing photoresponse of nanoparticulate α-Fe_2O_3 electrodes by surface composition tuning. *J. Phys. Chem. C* **2011**, *115*, 3497–3506. [CrossRef]
19. Al-Hajji, L.; Ismail, A.A.; Atitar, M.F.; Abdelfattah, I.; El-Toni, A.M. Construction of mesoporous g-C_3N_4/TiO_2 nanocrystals with enhanced photonic efficiency. *Ceram. Int.* **2019**, *45*, 1265–1272. [CrossRef]
20. Nasri, A.; Nezafat, Z.; Jaleh, B.; Orooji, Y.; Varma, R.S. Laser-assisted preparation of C3N4/Fe_2O_3/Au nanocomposite: A magnetic reusable catalyst for pollutant degradation. *Clean Technol. Environ. Policy* **2021**, *23*, 1797–1806. [CrossRef]
21. Guo, H.; Chen, M.; Zhong, Q.; Wang, Y.; Ma, W.; Ding, J. Synthesis of Z-scheme α-Fe_2O_3/g-C_3N_4 composite with enhanced visible-light photocatalytic reduction of CO_2 to CH_3OH. *J. CO_2 Util.* **2019**, *33*, 233–241. [CrossRef]
22. Shen, Y.; Han, Q.; Hu, J.; Gao, W.; Wang, L.; Yang, L.; Gao, C.; Shen, Q.; Wu, C.; Wang, X. Artificial trees for artificial photosynthesis: Construction of dendrite-structured α-Fe_2O_3/g-C_3N_4 Z-Scheme system for efficient CO_2 reduction into solar fuels. *ACS Appl. Energy Mater.* **2020**, *3*, 6561–6572. [CrossRef]

23. Duan, B.; Mei, L. A Z-scheme Fe_2O_3/g-C_3N_4 heterojunction for carbon dioxide to hydrocarbon fuel under visible illuminance. *J. Colloid Interface Sci.* **2020**, *575*, 265–273. [CrossRef] [PubMed]
24. Theerthagiri, J.; Senthil, R.; Priya, A.; Madhavan, J.; Michael, R.; Ashokkumar, M. Photocatalytic and photoelectrochemical studies of visible-light active α-Fe_2O_3–g-C_3N_4 nanocomposites. *RSC Adv.* **2014**, *4*, 38222–38229. [CrossRef]
25. Alduhaish, O.; Ubaidullah, M.; Al-Enizi, A.M.; Alhokbany, N.; Alshehri, S.M.; Ahmed, J. Facile Synthesis of Mesoporous α-Fe_2O_3 @ g-C_3N_4-NCs for Efficient Bifunctional Electro-catalytic Activity (OER/ORR). *Sci. Rep.* **2019**, *9*, 1–10. [CrossRef] [PubMed]
26. Kadi, M.W.; Mohamed, R.M.; Ismail, A.A.; Bahnemann, D.W. Performance of mesoporous α-Fe_2O_3/g-C_3N_4 heterojunction for photoreduction of Hg (II) under visible light illumination. *Ceram. Int.* **2020**, *46*, 23098–23106. [CrossRef]
27. Xu, Q.; Zhu, B.; Jiang, C.; Cheng, B.; Yu, J. Constructing 2D/2D Fe_2O_3/g-C_3N_4 direct Z-scheme photocatalysts with enhanced H_2 generation performance. *Sol. RRL* **2018**, *2*, 1800006. [CrossRef]
28. Jiang, Z.; Wan, W.; Li, H.; Yuan, S.; Zhao, H.; Wong, P.K. A Hierarchical Z-Scheme α-Fe_2O_3/g-C_3N_4 Hybrid for Enhanced Photocatalytic CO_2 Reduction. *Adv. Mater.* **2018**, *30*, 1706108. [CrossRef]
29. Padervand, M.; Rhimi, B.; Wang, C. One-pot synthesis of novel ternary $Fe_3N/Fe_2O_3/C_3N_4$ photocatalyst for efficient removal of rhodamine B and CO_2 reduction. *J. Alloys Compd.* **2021**, *852*, 156955. [CrossRef]
30. Liu, J.; Zhang, T.; Wang, Z.; Dawson, G.; Chen, W. Simple pyrolysis of urea into graphitic carbon nitride with recyclable adsorption and photocatalytic activity. *J. Mater. Chem.* **2011**, *21*, 14398–14401. [CrossRef]
31. Wang, J.; Qin, C.; Wang, H.; Chu, M.; Zada, A.; Zhang, X.; Li, J.; Raziq, F.; Qu, Y.; Jing, L. Exceptional photocatalytic activities for CO_2 conversion on AlO bridged g-C_3N_4/α-Fe_2O_3 z-scheme nanocomposites and mechanism insight with isotopesZ. *Appl. Catal. B Environ.* **2018**, *221*, 459–466. [CrossRef]
32. Khurram, R.; Wang, Z.; Ehsan, M.F. α-Fe_2O_3-based nanocomposites: Synthesis, characterization, and photocatalytic response towards wastewater treatment. *Environ. Sci. Pollut. Res.* **2021**, *28*, 17697–17711. [CrossRef] [PubMed]
33. Suwanboon, S.; Amornpitoksuk, P.; Muensit, N. Dependence of photocatalytic activity on structural and optical properties of nanocrystalline ZnO powders. *Ceram. Int.* **2011**, *37*, 2247–2253. [CrossRef]
34. Wang, X.; Sø, L.; Su, R.; Wendt, S.; Hald, P.; Mamakhel, A.; Yang, C.; Huang, Y.; Iversen, B.B.; Besenbacher, F. The influence of crystallite size and crystallinity of anatase nanoparticles on the photo-degradation of phenol. *J. Catal.* **2014**, *310*, 100–108. [CrossRef]
35. Devi, L.G.; Murthy, B.N.; Kumar, S.G. Photocatalytic activity of TiO_2 doped with Zn^{2+} and V^{5+} transition metal ions: Influence of crystallite size and dopant electronic configuration on photocatalytic activity. *Mater. Sci. Eng. B* **2010**, *166*, 1–6. [CrossRef]
36. Huang, Y.; Wang, Y.; Bi, Y.; Jin, J.; Ehsan, M.F.; Fu, M.; He, T. Preparation of 2D hydroxyl-rich carbon nitride nanosheets for photocatalytic reduction of CO_2. *RSC Adv.* **2015**, *5*, 33254–33261. [CrossRef]
37. Zhang, G.; Zhang, M.; Ye, X.; Qiu, X.; Lin, S.; Wang, X. Iodine modified carbon nitride semiconductors as visible light photocatalysts for hydrogen evolution. *Adv. Mater.* **2014**, *26*, 805–809. [CrossRef]
38. Hao, Q.; Mo, Z.; Chen, Z.; She, X.; Xu, Y.; Song, Y.; Ji, H.; Wu, X.; Yuan, S.; Xu, H. 0D/2D Fe_2O_3 quantum dots/g-C_3N_4 for enhanced visible-light-driven photocatalysis. *Colloids Surf. A Physicochem. Eng. Asp.* **2018**, *541*, 188–194. [CrossRef]
39. Thomas, A.; Fischer, A.; Goettmann, F.; Antonietti, M.; Müller, J.-O.; Schlögl, R.; Carlsson, J.M. Graphitic carbon nitride materials: Variation of structure and morphology and their use as metal-free catalysts. *J. Mater. Chem.* **2008**, *18*, 4893–4908. [CrossRef]
40. Khurram, R.; Wang, Z.; Ehsan, M.F.; Peng, S.; Shafiq, M.; Khan, B. Synthesis and characterization of an α-Fe_2O_3/ZnTe heterostructure for photocatalytic degradation of Congo red, methyl orange and methylene blue. *RSC Adv.* **2020**, *10*, 44997–45007. [CrossRef]
41. Li, Y.-P.; Li, F.-T.; Wang, X.-J.; Zhao, J.; Wei, J.-N.; Hao, Y.-J.; Liu, Y. Z-scheme electronic transfer of quantum-sized α-Fe_2O_3 modified g-C_3N_4 hybrids for enhanced photocatalytic hydrogen production. *Int. J. Hydrogen Energy* **2017**, *42*, 28327–28336. [CrossRef]
42. Sun, S.; Ji, C.; Wu, L.; Chi, S.; Qu, R.; Li, Y.; Lu, Y.; Sun, C.; Xue, Z. Facile one-pot construction of α-Fe_2O_3/g-C_3N_4 heterojunction for arsenic removal by synchronous visible light catalysis oxidation and adsorption. *Mater. Chem. Phys.* **2017**, *194*, 1–8. [CrossRef]
43. Zhang, Y.; Zhang, D.; Guo, W.; Chen, S. The α-Fe_2O_3/g-C_3N_4 heterostructural nanocomposites with enhanced ethanol gas sensing performance. *J. Alloys Compd.* **2016**, *685*, 84–90. [CrossRef]
44. Lee, S.; Park, J.-W. Hematite/graphitic carbon nitride nanofilm for fenton and photocatalytic oxidation of methylene blue. *Sustainability* **2020**, *12*, 2866. [CrossRef]
45. Bai, J.; Xu, H.; Chen, G.; Lv, W.; Ni, Z.; Wang, Z.; Yang, J.; Qin, H.; Zheng, Z.; Li, X. Facile fabrication of α-Fe_2O_3/porous g-C_3N_4 heterojunction hybrids with enhanced visible-light photocatalytic activity. *Mater. Chem. Phys.* **2019**, *234*, 75–80. [CrossRef]
46. Christoforidis, K.C.; Montini, T.; Bontempi, E.; Zafeiratos, S.; Jaén, J.J.D.; Fornasiero, P. Synthesis and photocatalytic application of visible-light active β-Fe_2O_3/g-C_3N_4 hybrid nanocomposites. *Appl. Catal. B Environ.* **2016**, *187*, 171–180. [CrossRef]
47. Liu, X.; Jin, A.; Jia, Y.; Jiang, J.; Hu, N.; Chen, X. Facile synthesis and enhanced visible-light photocatalytic activity of graphitic carbon nitride decorated with ultrafine Fe_2O_3 nanoparticles. *RSC Adv.* **2015**, *5*, 92033–92041. [CrossRef]
48. Argyle, M.D.; Bartholomew, C.H. Heterogeneous catalyst deactivation and regeneration: A review. *Catalysts* **2015**, *5*, 145–269. [CrossRef]
49. Ghane, N.; Sadrnezhaad, S. Combustion synthesis of g-C_3N_4/Fe_2O_3 nanocomposite for superior photoelectrochemical catalytic performance. *Appl. Surf. Sci.* **2020**, *534*, 147563. [CrossRef]
50. Paul, D.R.; Gautam, S.; Panchal, P.; Nehra, S.P.; Choudhary, P.; Sharma, A. ZnO-modified g-C_3N_4: A potential photocatalyst for environmental application. *ACS Omega* **2020**, *5*, 3828–3838. [CrossRef]

51. Zeng, S.; Tang, K.; Li, T.; Liang, Z.; Wang, D.; Wang, Y.; Zhou, W. Hematite hollow spindles and microspheres: Selective synthesis, growth mechanisms, and application in lithium ion battery and water treatment. *J. Phys. Chem. C* **2007**, *111*, 10217–10225. [CrossRef]
52. Zhu, W.; Cui, X.; Liu, X.; Zhang, L.; Huang, J.-Q.; Piao, X.; Zhang, Q. Hydrothermal evolution, optical and electrochemical properties of hierarchical porous hematite nanoarchitectures. *Nanoscale Res. Lett.* **2013**, *8*, 1–14. [CrossRef] [PubMed]